Collision cascades overlapping with self-interstitial defect clusters in Fe and W

J Byggmästar[1], **F Granberg**[1], **A E Sand**[1], **A Pirttikoski**[1], **R Alexander**[2], **M-C Marinica**[3], **K Nordlund**[1]

[1] Department of Physics, P.O. Box 43, FIN-00014, University of Helsinki, Finland
[2] UMET, UMR 8207, ENSCL, U Lille, 59655 Villeneuve d'Ascq Cédex, France
[3] DEN-Service de Recherches de Métallurgie Physique, CEA, Université Paris-Saclay, F-91191 Gif-sur-Yvette, France

E-mail: jesper.byggmastar@helsinki.fi

Abstract.
Overlap of collision cascades with previously formed defect clusters become increasingly likely at radiation doses typical for materials in nuclear reactors. Using molecular dynamics, we systematically investigate the effects of different pre-existing self-interstitial clusters on the damage produced by an overlapping cascade in bcc iron and tungsten. We find that the number of new Frenkel pairs created in direct overlap with an interstitial cluster is reduced to essentially zero, when the size of the defect cluster is comparable to that of the disordered cascade volume. We develop an analytical model for this reduced defect production as a function of the spatial overlap between a cascade and a defect cluster of a given size. Furthermore, we discuss cascade-induced changes in the morphology of self-interstitial clusters, including transformations between $1/2\langle 1\,1\,1 \rangle$ and $\langle 1\,0\,0 \rangle$ dislocation loops in iron and tungsten, and between C15 clusters and dislocation loops in iron. Our results provide crucial new cascade-overlap effects to be taken into account in multi-scale modelling of radiation damage in bcc metals.

Keywords: cascade overlap, iron, tungsten, molecular dynamics, dislocation loop

1. Introduction

Radiation damage in fission and fusion-relevant bcc metals has been studied for decades in both experimental and modelling work. The samples studied in experiments are typically irradiated up to doses of several displacements per atom (dpa) [1, 2, 3, 4]. The damage dose in the wall materials of current and future fission and fusion reactor wall materials can reach tens or hundreds of dpa [5, 6, 7]. At these doses, the density of defects is so high that subsequent collision cascades are likely to overlap with previously formed interstitial- and vacancy-type defect clusters, such as dislocation loops. Nevertheless, simulations of collision cascades have almost exclusively focused on the damage produced in defect-free single crystals [8]. The damage produced in cascade simulations, using e.g. molecular dynamics, can be transferred to larger-scale simulations methods, such as various kinetic Monte Carlo or cluster dynamics models, to simulate the long-term accumulation and evolution of radiation damage [9, 10, 11, 12]. The accuracy of the long-term simulations therefore rely on the cascade damage input from simulations of collision cascades. Consequently, a physically accurate multi-scale model for radiation damage should incorporate the effects of cascades overlapping with pre-existing defects [13].

Among the extensive literature on cascade simulations using molecular dynamics (MD), only a few studies on the effects of cascade overlap in bcc metals have been performed [14, 15, 16, 17]. All previous studies establish that the extent of the damage produced in cascade overlap is significantly reduced compared to cascades in a defect-free material. Gao et al. simulated low-energy (0.4–5 keV) cascades overlapping with the debris of a previous cascade in iron [14]. Stoller et al. performed a similar study at slightly higher primary knock-on atom (PKA) energies (10 keV) [15]. Both studies revealed a clear reduction in the amount of surviving point defects due to cascade overlap. Terentyev et al. carried out a set of simulations on interstitial-type dislocation loops in iron [16]. They reported that although the amount of new damage in cascade overlap with dislocation loops is generally reduced, the distribution of point defects and the final size of the pre-existing loop is dependent on whether the cascade dissolves the loop or not. Recently, we investigated the overlap effects for high-energy cascades in iron (50 keV) and tungsten (150 keV), where secondary cas-

cades were initiated on top of the debris of a previous cascade [17]. We observed a clear reduction in the amount of new defects in overlapping cascades, also at these higher energies, in both Fe and W. Furthermore, formation of more complex, immobile defect clusters were observed, when cascades overlapped with larger pre-existing defect clusters.

Self-interstitial atoms in bcc metals cluster together mainly in the form of dislocation loops with the Burgers vectors $1/2\langle 1\,1\,1\rangle$ and $\langle 1\,0\,0\rangle$. In iron, however, self-interstitial clusters exhibiting the C15 Laves phase have been theoretically predicted as the most stable interstitial-type cluster at small sizes [18]. The C15-type clusters can form directly in collision cascades and become energetically unstable compared to dislocation loops at sizes of around 50 interstitial atoms [19]. Acting as stationary traps for mobile dislocations, they can have a strong impact on the evolution of the defect structure in iron-based alloys, as observed in previous atomistic simulations [20, 21].

Both $1/2\langle 1\,1\,1\rangle$ and $\langle 1\,0\,0\rangle$ dislocation loops are readily observed in irradiation experiments of iron and tungsten [22, 2, 23, 24] and in MD simulations of tungsten [25], despite the $\langle 1\,0\,0\rangle$ loop being energetically unfavoured compared to $1/2\langle 1\,1\,1\rangle$ loops [19]. The populations of the two dislocation loops depend, however, on the irradiation conditions and type of irradiation (neutrons, electrons, or ions) [23]. In iron, the formation energy of $\langle 1\,0\,0\rangle$ loops decreases with temperature due to magnetic effects, and they become energetically more stable than $1/2\langle 1\,1\,1\rangle$ loops above temperatures around 600 K [26]. While experiments do show increasing fractions of $\langle 1\,0\,0\rangle$ loops at higher temperatures in iron [3], $\langle 1\,0\,0\rangle$ loops are also formed in low-temperature irradiations [23]. The dominating formation mechanism of the $\langle 1\,0\,0\rangle$ loops are therefore still actively debated. Several mechanisms have been proposed in the literature, either from combinations of two $1/2\langle 1\,1\,1\rangle$ dislocation loops [27, 28], spontaneous changes in the Burgers vector [29, 30], collapse of growing C15 clusters [31], or due to a shockwave in high-energy cascades [32]. Recently, we showed using MD simulations that formation of $\langle 1\,0\,0\rangle$ loops become increasingly likely at doses when cascade overlap is frequent, and form either through the earlier-proposed mechanisms or from partial cascade-overlap with mixed dislocation networks [33].

In this work, we systematically and compre-

hensively study the effects of cascade overlap on interstitial-type clusters for low-energy (below the sub-cascade threshold) cascades in both iron and tungsten. We initiate cascades on or close to interstitial-type clusters of a size and type typical to those formed directly in cascades. In tungsten, these clusters include the $1/2\langle 1\,1\,1\rangle$ and $\langle 1\,0\,0\rangle$ dislocation loops. In iron, we also study overlap on the highly stable C15 cluster. We analyse the extent of the surviving damage as a function of the spatial overlap between the cascade and the pre-existing cluster. The results are combined into a simple analytical model for predicting the defect production in cascade overlap. Additionally, we investigate cascade-induced changes in the morphology of the pre-existing cluster. This includes changes in the Burgers vector of dislocation loops, collapse of C15 clusters into loops, and changes in cluster size. Our observations provide valuable input for incorporating overlap effects in higher-scale simulations of radiation damage.

2. Methods

2.1. Simulation details

All simulations were carried out using the classical molecular dynamics code PARCAS [34, 35], with several different embedded atom method interatomic potentials suitable for cascade simulations. For iron, we used the well-established potential by Ackland et al. [36], hereafter denoted AM04. Additionally, we used the potential by Marinica [18, 37], denoted M07, which correctly reproduces the C15 Laves phase cluster as the most stable interstitial cluster at small and medium sizes [18]. The M07 potential was recently modified to be more accurate at short distances (and hence more suitable for cascade simulations) while retaining all defect and equilibrium properties of the original M07 potential [21]. We also carried out simulations using this modified M07 potential, denoted M07-B. For tungsten, we used the potential by Ackland and Thetford [38], with the short-range modification by Zhong et al. [39], denoted AT-ZN. We also used the potential by Derlet et al. [40] with the short-range connection to the ZBL potential [41] by Björkas et al. [42], denoted DND-BN. Additionally, we repeated the simulations using the potential by Marinica et al. [43] (the version therein referred to as EAM4) with the short-range modification by Sand et al. [44] (therein named M-S_h), here denoted M4-S. A comparison of some cascade-relevant properties between these potentials is provided in Appendix A and Appendix B.

Low-energy cascades, 3 and 5 keV in Fe and 10 and 30 keV in W, were initiated in systems containing a cluster of N_{SIA} self-interstitial atoms (SIA). The cluster sizes were chosen as those typically formed directly in cascades, or after a short thermal evolution. In Fe, we studied cluster sizes in the range $N_{\mathrm{SIA}} = 1$–50 and in W $N_{\mathrm{SIA}} = 1$–100. The disordered cascade regions formed at these PKA energies are larger than the pre-existing SIA cluster. Hence, when we refer to full overlap, the cascade has completely enveloped the pre-existing cluster. Clusters larger than about 15 SIA were introduced as $1/2\langle 1\,1\,1\rangle$ and $\langle 1\,0\,0\rangle$ dislocation loops and (in Fe) as C15 clusters. Smaller clusters of $N_{\mathrm{SIA}} = 1$–11 were embedded as parallel dumbbell configurations and (in Fe) as C15 clusters. The details of all pre-existing clusters used in the cascade simulations are summarised in table 1. The sizes of the simulation cells containing the SIA clusters were around 40 unit cells in each direction for Fe, 54 unit cells for 10 keV cascades in W, and around 70 unit cells for 30 keV cascades in W. The exact system sizes varied slightly depending on cluster type, as $1/2\langle 1\,1\,1\rangle$ dislocation loops were embedded in a box with the x, y, and z axes along the $[1\,\bar{1}\,0]$, $[\bar{1}\,\bar{1}\,2]$, and $[1\,1\,1]$ directions, respectively.

After relaxation to zero pressure and the desired temperature, cascades were initiated at different distances from the centre of the pre-existing cluster. The temperature was controlled at the borders of the system using a Berendsen thermostat [45]. Electronic stopping was applied as a friction term on atoms with kinetic energies above 1 eV in Fe [46] and above 10 eV in W [47, 48]. The simulation time for all cascades was 30 ps. The PKA was directed towards the centre of the pre-existing cluster, from a given distance in a uniformly distributed random crystal direction. The range of PKA-to-centre distances was chosen so that the complete overlap range was covered, i.e. from cascades fully overlapping with the pre-existing cluster up to the limit of no overlap. Initial PKA distances up to 50–60 Å proved to be sufficient for the PKA energies used here. At each PKA distance, 100–200 simulations were carried out to provide enough statistics. This resulted in 400–800 simulations for each energy, temperature, cluster size, cluster type, and potential, and in total several hundred thousand individual cascade simulations.

2.2. Analysis

After each cascade, the surviving damage was analysed. Interstitial atoms and vacancies were located using the Wigner-Seitz analysis method. The point defects were grouped into clusters to gather statistics on the final size of the pre-existing cluster. For the cluster analysis, we used cutoff radii between the second and third nearest neighbour for vacancies, and between the third and fourth nearest neighbour for interstitials [49]. The dislocation extraction algorithm implemented in OVITO was used to identify possible

Table 1: Summary of pre-existing interstitial clusters used in the cascade-overlap simulations. For each cluster type, size, temperature, PKA energy, and interatomic potential, around 400–800 cascade simulations were carried out. The PKA was initiated at different distances from the centre of the pre-existing cluster, ranging from 10 to 60 Å, in order to cover the full range of overlap.

Fe				
Cluster type	Size (N_{SIA})	T (K)	E_{PKA} (keV)	Potential
$1/2\langle 1\,1\,1 \rangle$ loop	14, 22, 26, 30, 48	0, 300	3, 5	AM04, M07-B, M07
$\langle 1\,0\,0 \rangle$ loop	16, 22, 26, 30, 48	0, 300	3, 5	AM04, M07-B, M07
C15	4, 11, 17, 30, 40, 50	0, 300	3, 5	M07-B, M07
$\langle 1\,1\,0 \rangle$ dumbbells	1, 2, 4	0	3, 5	M07-B
$\langle 1\,1\,1 \rangle$ dumbbells	6, 8, 10	0	3, 5	M07-B
W				
Cluster type	Size (N_{SIA})	T (K)	E_{PKA} (keV)	Potential
$1/2\langle 1\,1\,1 \rangle$ loop	18, 22, 30, 52, 104	0, 300	10	AT-ZN, DND-BN, M4-S
$1/2\langle 1\,1\,1 \rangle$ loop	30, 104	300	30	AT-ZN
$\langle 1\,0\,0 \rangle$ loop	16, 22, 30, 56, 104	0, 300	10	AT-ZN, DND-BN, M4-S
$\langle 1\,0\,0 \rangle$ loop	30, 104	300	30	AT-ZN
$\langle 1\,1\,1 \rangle$ dumbbells	1, 2, 3, 4, 6, 8, 10	0	10	AT-ZN
$\langle 1\,1\,1 \rangle$ dumbbells	1, 4, 10	0	30	AT-ZN

dislocation loops [50, 51]. In Fe, C15 clusters were identified by analysing the geometries of interstitial clusters. C15 clusters isolated with the Wigner-Seitz analysis consist of non-parallel $\langle 1\,1\,0 \rangle$ dumbbells, connected to form hexagonal and triangular rings of atoms lying in $\{1\,1\,1\}$ planes. By looking at the nearest-neighbour angles and the plane on which they lie, C15 or C15-like clusters can therefore be identified. This approach was previously used for identifying C15 clusters among large numbers of defect clusters in highly damaged systems [21], and proved to be fairly reliable.

The cascade-overlap effect on the number of new Frenkel pairs (FPs) and the size and type of the final cluster were analysed as a function of distance between the centre of the disordered cascade-induced molten region (at peak damage) and the centre of the pre-existing cluster. From now on we refer to this cascade–to–cluster distance as the *separation distance*. A separation distance of zero represents full overlap of the disordered cascade region with the pre-existing cluster. The limit of no overlap is reached at a separation distance given by the sum of the radii of the cluster and the cascade region. The centre of the disordered cascade region at peak damage was calculated as the geometrical centre of the liquid atoms, weighted by the kinetic energy of each atom. An atom was labelled liquid when the average kinetic energy of the atom and its neighbours was above the average kinetic energy at the melting point predicted by the potential, i.e. $\frac{3}{2}k_{\text{B}}T_{\text{melt}}$ [34]. Using the disordered group of atoms at peak damage, it is possible to obtain both a location

and size of the molten cascade region, and hence the extent of overlap. The average volume and radius of the cascade region is useful when interpreting and analysing the results. The volume of the cascade region was calculated by enclosing the disordered atoms by a surface mesh using OVITO. An effective average radius of the cascade at a given PKA energy and temperature was calculated by assuming a spherical cascade region (which, on average, is a good assumption for cascades well below the subcascade splitting threshold energy).

As is always true for cascade damage, the statistical variations are large, since individual cascades can vary significantly. In order to get reliable statistics, a large number of simulations was therefore necessary. Consequently, the results require careful statistical analysis in order to extract meaningful data and overall trends. Figure 1 shows a typical case for the number of new Frenkel pairs created in overlap with an existing SIA cluster, as a function of the separation distance. The data points, each corresponding to one cascade simulation with a calculated separation distance and a number of new Frenkel pairs, were grouped into bins with widths of 5 Å. Figure 1 shows the calculated mode, mean, and median values of each bin. The uncertainty of the mean values are the standard errors of the mean. Error bars of the median values are represented by the interquartile range (i.e. the 25% and 75% percentiles), showing the spread of the data. We chose to represent all data analysed as functions of separation distance using the median values of each bin, due to them being less sensitive to outliers than the mean values, and always uniquely defined, as opposed
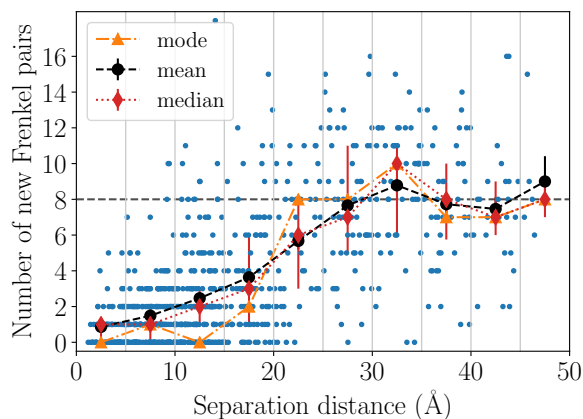
Figure 1: Example of the statistical spread and calculated mode, mean, and median values of the binned data for numbers of new Frenkel pairs created in overlapping cascades. Each small blue point is the result of one simulation. The data are from 10 keV cascades overlapping with a 30 SIA $1/2\langle 1\,1\,1 \rangle$ loop in W at 0 K, using the AT-ZN potential.

to the mode. Bins with poor statistics (fewer than ten data points) were excluded. Typically, each bin contains data from around 50–100 individual simulations.

3. Point defect production

Figure 1 shows the general trend and statistical variations of the number of new Frenkel pairs created in overlapping cascades, as a function of the separation distance. The horizontal dashed line indicates the median numbers of Frenkel pairs created in the corresponding defect-free material. Results from cascades in defect-free lattices are given in Appendix C. At maximum overlap (zero separation distance), the number of new Frenkel pairs is reduced to a minimum, typically a small fraction of the corresponding defect-free number. As the separation distance increases, and the cascade is only partially overlapping with the pre-existing cluster, the number of new Frenkel pairs increases, until it saturates to the value expected from simulations in the defect-free material.

Representative examples illustrating the effects of different simulation conditions in both Fe and W are shown in figure 2. Figure 2a shows the defect production for clusters of different type but same size. The data follows the same trend regardless of pre-existing cluster type, meaning that the reduction in new damage due to cascade overlap is not dependent on the type of the SIA cluster. For example, in Fe both types of dislocation loops follow the same curve as a C15 cluster, provided that they are comparable in size. This is expected in the case of full overlap (i.e. at short separation distances), as the cascade then completely dissolves the cluster into a molten region, and all information about the morphology of the original cluster is lost. However, even in the case of partial overlap, i.e. when the cascade region only partially dissolves the pre-existing cluster, the number of new surviving Frenkel pairs is the same regardless of cluster type in both Fe and W. In particular, overlap on three-dimensional C15 clusters results in the same defect production as planar loops at all separation distances, indicating that the dimensionality of the pre-existing cluster has no visible effect in the studied cluster size range.

Figure 2b shows examples of the defect production for the same cluster type of different sizes. For cascades with the same PKA energy, increasing the size of the pre-existing SIA cluster decreases the number of created Frenkel pairs at all separation distances, although the spread of the data is large. The size dependence on the decrease in numbers of new Frenkel pairs for fully overlapping cascades with different PKA energies is shown in figures 3–4 for Fe and W, respectively. In the lower figures of figures 3–4, the data points are normalised by the FP count in the defect-free material in the vertical axis, and by the size of the cascade volume in the horizontal axis. The normalised data overlaps completely (within the statistical uncertainty), indicating that the reduced number of new Frenkel pairs in cascade overlap can be estimated from figures 3–4 for any PKA energy, when considering the relative size of the defect cluster and the cascade region. In both Fe and W, the normalised data saturates to a value close to zero when the radius of the pre-existing SIA cluster is roughly half that of the disordered cascade region. The number of Frenkel pairs at the saturation size varies slightly between the interatomic potentials, but the overall trend is the same.

Figure 2c shows the difference in the defect production between 0 and 300 K. The temperature dependence on the overlap effect is weak. Cascades in W show no visible temperature dependence in the 0–300 K range, while a slight but statistically negligible decrease in the Frenkel pair counts is visible in Fe. The difference roughly corresponds to the decrease in surviving defect count in the defect-free material as the temperature is increased, and no differences in the cascade overlap behaviour is observed.

Increasing the PKA energy will naturally produce higher numbers of Frenkel pairs at all separation distances, as seen in figure 2d. The trend is otherwise similar. The saturation distance is increased corresponding to the increase in the molten cascade region. The PKA energy dependence on the numbers
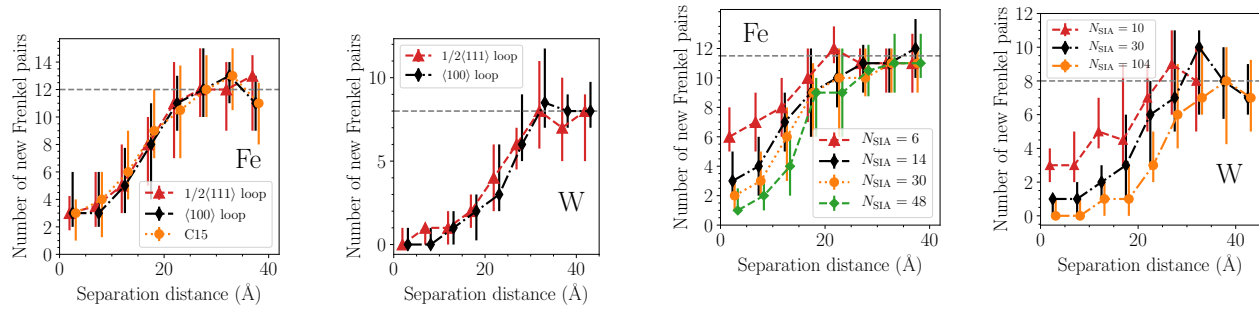
(a) Dependence on pre-existing cluster type. Fe: $E_{\mathrm{PKA}} = 5$ keV, $N_{\mathrm{SIA}} = 30$, $T = 300$ K, M07-B potential. W: $E_{\mathrm{PKA}} = 10$ keV, $N_{\mathrm{SIA}} = 104$, $T = 300$ K, AT-ZN potential.

(b) Dependence on pre-existing cluster size. Fe: $E_{\mathrm{PKA}} = 3$ keV, $1/2\langle 1\,1\,1 \rangle$ loops, $T = 0$ K, M07-B potential. W: $E_{\mathrm{PKA}} = 10$ keV, $1/2\langle 1\,1\,1 \rangle$ loops, $T = 0$ K, AT-ZN potential.
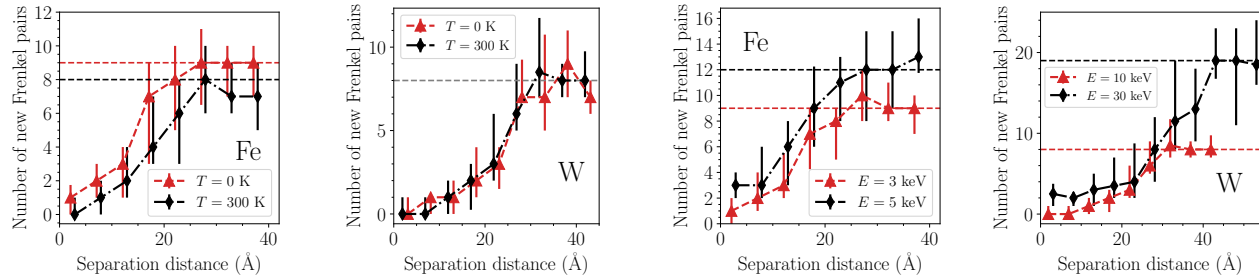
(c) Dependence on temperature. Fe: $E_{\mathrm{PKA}} = 3$ keV, $1/2\langle 1\,1\,1 \rangle$ loops, $N_{\mathrm{SIA}} = 48$, AM04 potential. W: $E_{\mathrm{PKA}} = 10$ keV, $\langle 1\,0\,0 \rangle$ loops, $N_{\mathrm{SIA}} = 104$, AT-ZN potential.

(d) Dependence on PKA energy. Fe: $1/2\langle 1\,1\,1 \rangle$ loops, $N_{\mathrm{SIA}} = 26$, $T = 0$ K, AM04 potential. W: $\langle 1\,0\,0 \rangle$ loops, $N_{\mathrm{SIA}} = 104$, $T = 300$ K, AT-ZN potential.
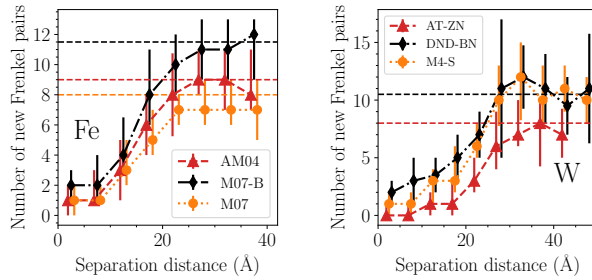
(e) Dependence on interatomic potential. Fe: $E_{\mathrm{PKA}} = 3$ keV, $\langle 1\,0\,0 \rangle$ loops, $N_{\mathrm{SIA}} = 48$, $T = 0$ K. W: $E_{\mathrm{PKA}} = 10$ keV, $1/2\langle 1\,1\,1 \rangle$ loops, $N_{\mathrm{SIA}} = 104$, $T = 0$ K

Figure 2: Examples of the reduced defect production for cascades overlapping with SIA clusters in iron and tungsten, as functions of separation distance (i.e the centre-to-centre distance between the pre-existing cluster and the disordered cascade region). Simulation details are given below each figure. Each data point is the median value in a bin containing in the order of 50–100 simulations. The horizontal lines show the median number of Frenkel pairs in cascades in the defect-free material. The error bars show the interquartile range, i.e. the spread of the data around the median. The data points are slightly shifted in the x axis direction to make the error bars visible.
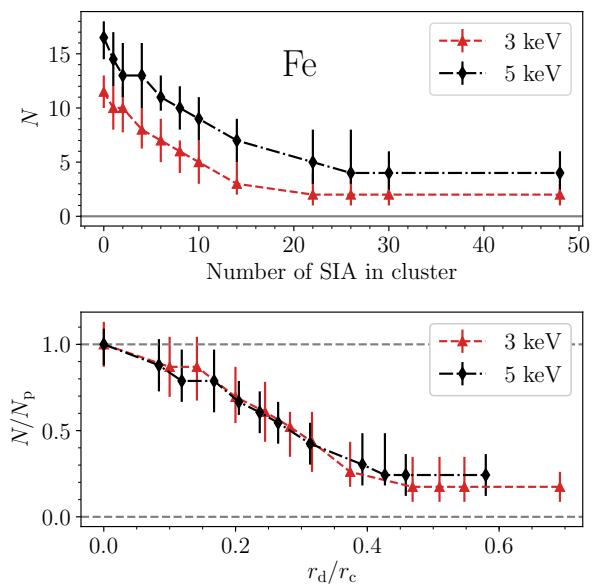
Figure 3: Upper: numbers of new Frenkel pairs created in fully overlapping cascades as a function of the size of the pre-existing SIA cluster in Fe and the M07-B potential. Lower: normalised data showing relative numbers of Frenkel pairs as a function of relative size of the pre-existing cluster to the disordered cascade region. N_p is the number of Frenkel pairs produced in cascades in the defect-free material, r_d is the radius of the SIA cluster, and r_c is the approximate radius of the disordered cascade region at peak damage.
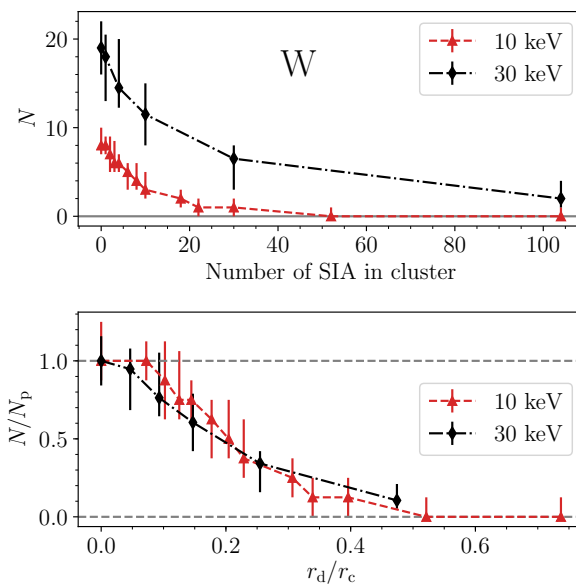
Figure 4: Upper: numbers of new Frenkel pairs created in fully overlapping cascades as a function of the size of the pre-existing SIA cluster in W and the AT-ZN potential. Lower: normalised data showing relative numbers of Frenkel pairs as a function of relative size of the pre-existing cluster to the disordered cascade region. N_p is the number of Frenkel pairs produced in cascades in the defect-free material, r_d is the radius of the SIA cluster, and r_c is the approximate radius of the disordered cascade region at peak damage.

of new FPs at full overlap is also shown in figures 3–4, as discussed above.

Finally, figure 2e shows examples of the differences in the reduced FP production in different interatomic potentials. Apart from the different numbers of Frenkel pairs in the defect-free material (i.e. the limit of no overlap), the main difference is the surviving numbers of Frenkel pairs at full overlap. All other trends discussed above are true regardless of potential.

4. Analytical model for point defect production

In order to incorporate the effects of cascade overlap on the defect production in larger-scale simulation methods, it would be useful to develop an approximate model for the overlap effect as a function of separation distance. The model should correctly reproduce all trends discussed above, in order to allow predicting the numbers of new Frenkel pairs in cascade overlap with a given SIA cluster at a given PKA energy and temperature. Due to the chaotic nature of collision cascades, any model predicting the surviving damage

will naturally only be approximately accurate. It is therefore our goal to construct a model as general as possible, that captures the correct overlap behaviour without relying on numerical fitting to approximate data or specific features of the interatomic potential.

Following simple arguments, all trends discussed previously for the reduced defect production in cascade overlap with SIA clusters can be combined into an approximate analytical function. The function should satisfy the following conditions. Firstly, the number of new Frenkel pairs created in cascade overlap (N) should reach the corresponding number produced in cascades in the defect-free material (N_p) when the cascade no longer overlaps with the pre-existing cluster, i.e. at a separation distance of around $r_d + r_c$. Here, r_d is the radius of the defect cluster and r_c is the radius of the molten cascade region at peak damage. Secondly, for a given PKA energy, increasing the size of the SIA cluster should decrease the number of new Frenkel pairs at all separation distances, as observed in the previous section. Finally, at full overlap (zero separation distance), the number of new Frenkel pairs is typically a small fraction of the expected FP
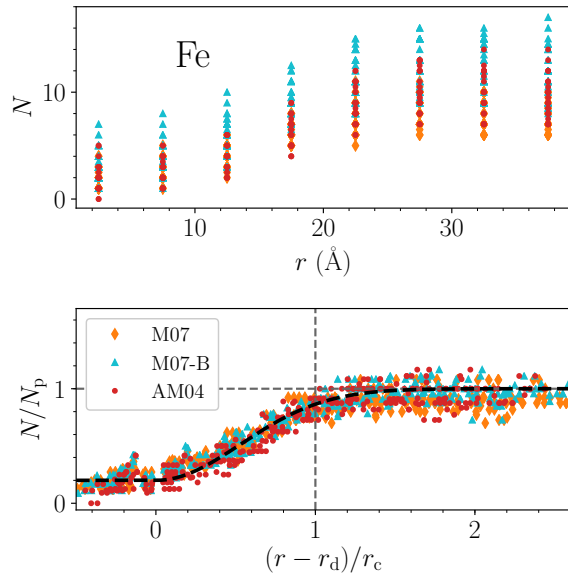
Figure 5: Upper: simulation data for the numbers of new Frenkel pairs as functions of separation distance in Fe. Lower: normalised data compared to the analytical model. See the text for details.
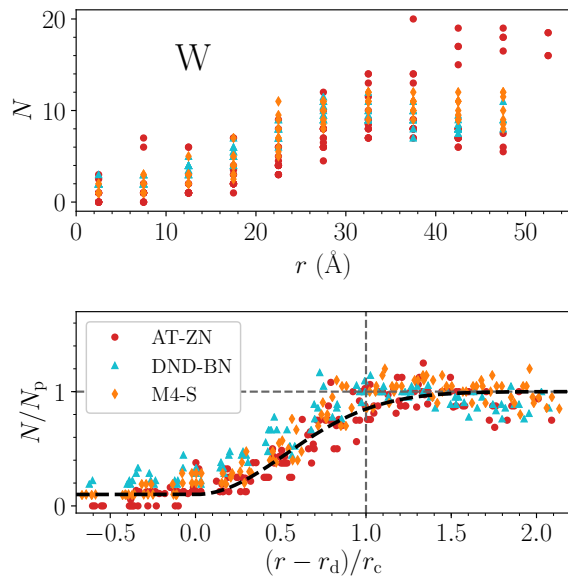

Figure 6: Upper: simulation data for the numbers of new Frenkel pairs as functions of separation distance in W. Lower: normalised data compared to the analytical model. See the text for details.

count in the defect-free material (N_{p}). We will call this full-overlap Frenkel pair count N_0, which is a parameter depending primarily on the relative size of the cascade region and the pre-existing cluster, as shown in figures 3–4. As is clear from figure 2, the general shape of the data can be captured with any sigmoid function. However, a simple symmetric sigmoid function starting from zero separation distance and saturating towards the maximum value at the limit of no overlap will not satisfy the second condition given above. That is, it will not reproduce the correct size dependence (increasing the defect cluster size will symmetrically "stretch" the sigmoid curve towards zero and the increased limit of no overlap, which incorrectly results in higher numbers of Frenkel pairs at low separation distances compared to a smaller cluster).

A simple function that satisfies the above conditions, and therefore reproduces all observed and expected trends is

$$N = \begin{cases} N_0 & , r < r_{\mathrm{d}} \\ N_{\mathrm{p}} - (N_{\mathrm{p}} - N_0) \exp\left[-\dfrac{(r - r_{\mathrm{d}})^2}{(a r_{\mathrm{c}})^2}\right] & , r \geq r_{\mathrm{d}}. \end{cases} \quad (1)$$

Here, the sigmoid function (given by an exponential function) is shifted according to the size of the pre-existing defect cluster to reproduce the correct size dependence. A similar exponential function was used by Gao et al. for describing overlap with debris from a previous cascade [14]. The saturation distance is defined by the constant a. We fix $a = 0.75$, which results in a limit of no overlap at a distance slightly above $r_{\mathrm{d}} + r_{\mathrm{c}}$, in agreement with the simulation data. We stress that, after the general choice of a, Eq. 1 contains no free fitting parameters. The dependence on temperature, PKA energy, and interatomic potential are all implicitly accounted for in the values of N_{p} and r_{c}, which are readily available from simulations of cascades in the defect-free material (see Appendix C). Naturally, these values will be different in different interatomic potentials, and can be chosen either as approximate values or values given by a specific potential. The only parameter needed from cascade-overlap data is N_0, which can be estimated from figures 3–4 for any PKA energy below the subcascade-splitting threshold. However, as discussed previously, for sufficiently large pre-existing SIA clusters, N_0 is very close to zero in both Fe and W.

The only variable defining the overlap between the cascade region and the pre-existing cluster in both our simulation data and the analytical model is the separation distance. That is, we have not included any dependence on the position of the cascade region with respect to the geometrical features of the pre-existing cluster, such as the habit plane of
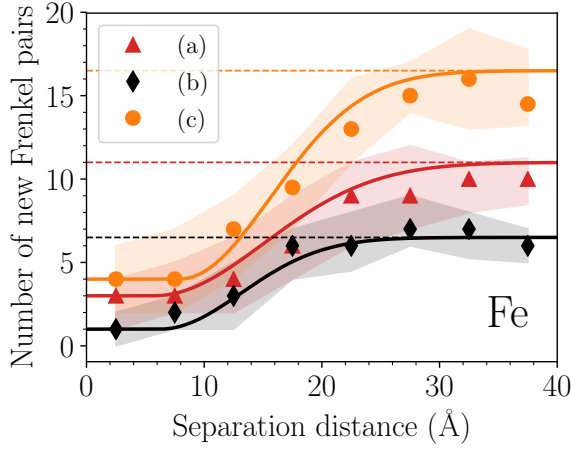
Figure 7: Examples comparing the analytical model with data from cascade-overlap simulations in Fe. The shaded areas show the statistical spread in the data. Case (a) is for 5 keV cascades on a pre-existing 22 SIA $1/2\langle 1\,1\,1\rangle$ loop at 300 K in the AM04 potential. Case (b) is: 3 keV, 30 SIA $\langle 1\,0\,0\rangle$ loop, 300 K in M07, and case (c): 5 keV, 48 SIA $\langle 1\,0\,0\rangle$ loop, 0 K in M07-B.
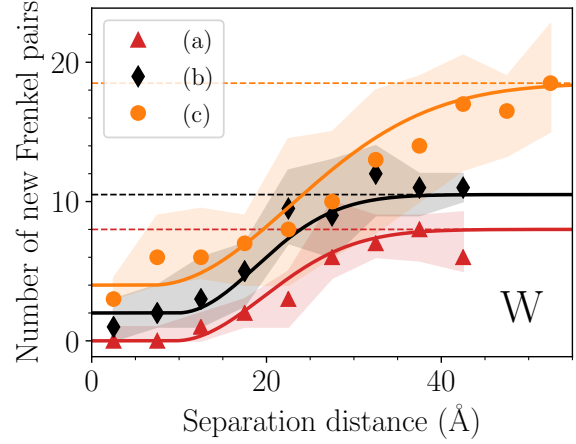
Figure 8: Examples comparing the analytical model with data from cascade-overlap simulations in W. The shaded areas show the statistical spread in the data. Case (a) is for 10 keV cascades on a pre-existing 56 SIA $\langle 1\,0\,0\rangle$ loop at 300 K in the AT-ZN potential. Case (b) is: 10 keV, 52 SIA $1/2\langle 1\,1\,1\rangle$ loop, 0 K in M4-S, and case (c): 30 keV, 30 SIA $\langle 1\,0\,0\rangle$ loop, 300 K in AT-ZN.

a dislocation loop. For example, we have made no distinction between whether the cascade region is located in an in-plane or out-of-plane direction from the loop centre. This effectively means that we assume all SIA clusters, including dislocation loops, to be spherical with a volume corresponding to the radius of the cluster. This is justified by the observation in the previous section that the dimensionality of the pre-existing cluster, i.e. C15 clusters compared to dislocation loops, has no visible effect on the average defect production (in the cluster size range considered here). Additionally, spherical clusters are also typically assumed in object kinetic Monte Carlo models [12], which makes our model directly applicable to the SIA clusters considered in larger-scale modelling methods. As previously mentioned, the cascade region is also assumed to be spherical, which on average is a good approximation at low PKA energies, when the cascade does not split into multiple subcascades. However, the model could also be used for PKA energies above the subcascade threshold by considering the volumes of individual subcascades [52, 53].

When comparing the model to the data, it is useful to normalise the exponential part as

$$\frac{N}{N_{\mathrm{p}}} = 1 - (1 - N_0')\exp\left(-\frac{r'^2}{a^2}\right), r' > 0, \qquad (2)$$

where $N_0' = N_0/N_{\mathrm{p}}$ and $r' = (r - r_{\mathrm{d}})/r_{\mathrm{c}}$. In this way, the data should reach the limit of no overlap ($N/N_{\mathrm{p}} = 1$) at $r' = 1$ for all cases. Negative values of r' correspond to the maximum-overlap range

where N/N_{p} is assumed to be constant (N_0'), as in Eq. 1. Figures 5–6 show the raw simulation data of the defect production for all pre-existing loop types, temperatures, PKA energies, and interatomic potentials for Fe and W, respectively. In the lower figures, the data is normalised in order to compare all data with the analytical model using Eq. 2. Despite normalising the data, the value of N_0' is still dependent on the size of the pre-existing cluster. Figures 5–6 therefore only includes sizes above 14 SIA for Fe and 30 SIA for W, to be able to use a single approximate value of N_0' for all data. For Fe, we used $N_0' = 0.2$ and for W, $N_0' = 0.1$. However, using $N_0' = 0$ for all cases still results in a satisfactory agreement with the data. The values of the cascade radii (r_{c}) and the defect-free FP count (N_{p}) are provided in Appendix C.

Figures 7–8 show a few representative examples of the defect production predicted by the analytical model compared with the simulation data. The shown examples include data from different types of pre-existing cluster, different size, temperature, PKA energy and interatomic potential. The shaded regions highlight the statistical spread in the data, given by the interquartile range of the median values. The values of N_0 are obtained from figures 3–4. In all cases in both Fe and W, the model reproduces the simulation data within the statistical uncertainty.
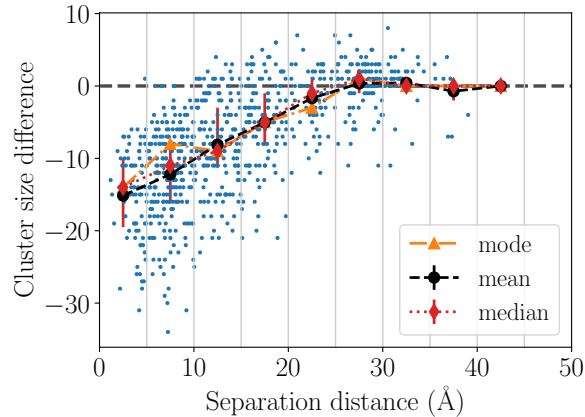
Figure 9: Example of the difference between the size of the final and the initial SIA cluster after an overlapping cascade, illustrating the statistical spread of the data. Blue data points are the results from individual simulations, which are grouped into bins with the mode, mean, and median values plotted. The data are from 5 keV cascades on a 48 SIA $1/2\langle 1\,1\,1\rangle$ loop at 0 K in Fe, with the M07-B potential.

5. Cascade-induced changes in cluster morphology

5.1. Changes in cluster size

Figure 9 shows the difference in size between the final and initial SIA cluster after overlapping cascades for a typical case. The SIA cluster generally shrinks as a result of the overlapping cascade. Additionally, figure 9 shows the statistical spread in the collected data, illustrating that even though the size of the SIA cluster is most likely to decrease or remain constant, the cluster can also grow by absorbing new SIAs at distances of partial overlap.

The decrease in size in terms of numbers of SIAs is almost constant for a given PKA energy, regardless of size of the initial SIA cluster. This is especially true in Fe for all interatomic potentials. In W, a slight dependence on the SIA cluster size is observed, although the statistical uncertainties are large. Figure 10 shows the number of SIAs lost from the cluster due to the overlapping cascade for different cluster sizes. All cluster types and all interatomic potentials show a similar behaviour, although the maximum decrease in cluster size at full overlap varies slightly between the potentials and the different temperatures. The slight cascade-induced growth of the SIA cluster at larger separation distances is more pronounced in W, although the statistical spread is large.
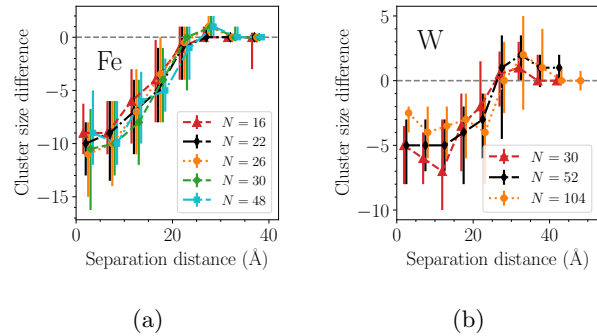

(a)   (b)

Figure 10: Examples of the difference between the size of the original pre-existing SIA cluster and the final SIA cluster after an overlapping cascade. The Fe (a) data are from 5 keV cascades on $\langle 1\,0\,0\rangle$ loops at 300 K in the M07-B potential. The W (b) data are from 10 keV cascades on $1/2\langle 1\,1\,1\rangle$ loops at 300 K in the AT-ZN potential. The data points are slightly shifted to make the error bars visible.
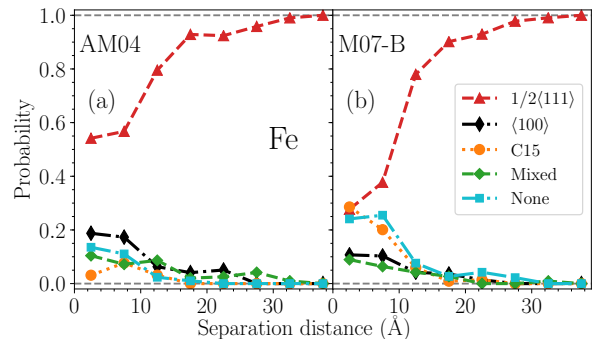

Figure 11: Example of the observed probabilities of forming different types of SIA clusters as functions of separation distance in Fe. The data is from 3 keV cascades overlapping with a 30 SIA $1/2\langle 1\,1\,1\rangle$ loop at 300 K, for both the AM04 and M07-B potentials.

5.2. Changes in cluster type

Fully or partially overlapping cascades can trigger changes in the type of the pre-existing cluster. Figure 11 shows examples of the probabilities (fractions of all simulations at each binned separation distance) of forming different types of clusters in Fe due to an overlapping cascade, compared between the AM04 and M07-B potentials. Only the pre-existing cluster and its morphology after the overlapping cascade is considered in the analysis. The cluster morphology is separated into five categories, the three main types: $1/2\langle 1\,1\,1\rangle$ loops, $\langle 1\,0\,0\rangle$ loops, C15 clusters, and two additional categories: mixed clusters, and "None", the latter meaning that the cluster was not identified as any specific type. Mixed clusters are any cluster

(a) Mixed dislocation loop.

(b) Mixed dislocation loop attached to small C15-like clusters.

(c) $1/2\langle 1\,1\,1\rangle$ loop segment terminating in a C15 cluster.

(d) $\langle 1\,0\,0\rangle$ loop attached to a C15 cluster.
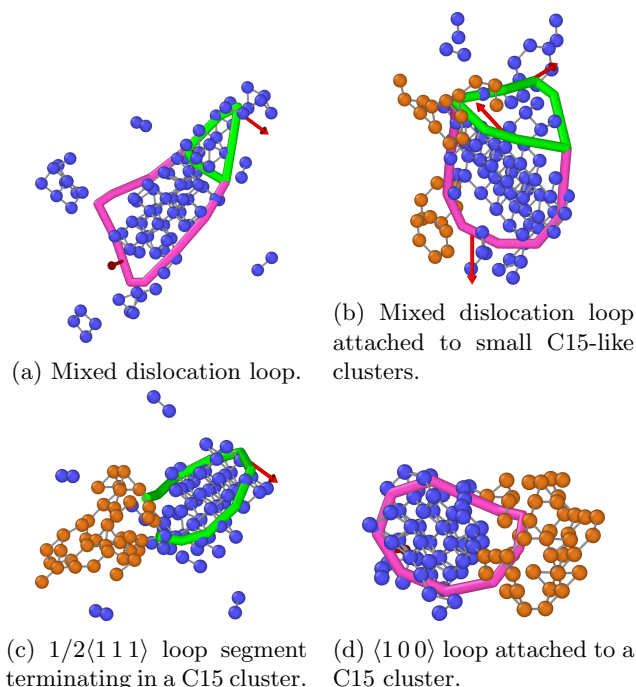
Figure 12: Examples of different "mixed" interstitial clusters observed in Fe after an overlapping cascade in the M07-B potential. The self-interstitial atoms are shown as bonded dumbbell configurations, i.e. two atoms for each SIA. Orange atoms highlight C15-like clusters, other SIAs are blue. Green lines are $1/2\langle 1\,1\,1\rangle$ dislocation lines and magenta lines are $\langle 1\,0\,0\rangle$ dislocations. The red arrows show the directions of the Burgers vectors. All clusters contain roughly 50 SIAs and are 1.5–2 nm in width.

identified as containing parts of more than one of the above categories. Some examples of clusters defined as mixed clusters in Fe are shown in figure 12. These include dislocation loops with segments of both Burgers vectors, dislocations that do not form closed loops but instead terminate in a C15 cluster or any other defect cluster, or dislocation loops attached to C15 clusters. Figure 13 shows examples of mixed clusters in W, which mainly are dislocation loops with segments of both Burgers vectors. Similar complex clusters were also previously observed in overlap of high-energy cascades [17]. Tests showed that some of these mixed clusters are unstable and rearrange into perfect dislocation loops of either type after a short annealing simulation. Other remained as "mixed" clusters even after annealing at 1000 K for 1 ns. However, systematically assessing the stability of these complex defect structures is beyond the scope of this work.

The pre-existing cluster in figure 11 is a $1/2\langle 1\,1\,1\rangle$ loop containing 30 SIAs. In the AM04 potential, the

(a) Intertwined $1/2\langle 1\,1\,1\rangle$ loop.

(b) Mixed dislocation loop with dividing $1/2\langle 1\,1\,1\rangle$ screw segment.

(c) Mixed dislocation loop network.

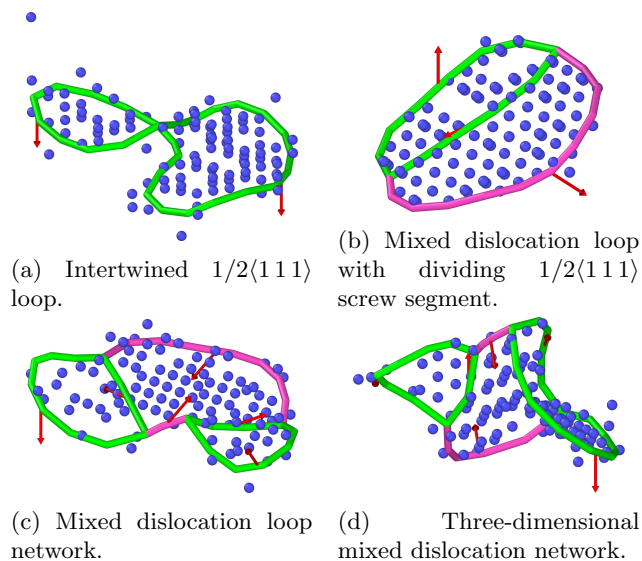(d) Three-dimensional mixed dislocation network.

Figure 13: Examples of different "mixed" interstitial clusters observed in W after an overlapping cascade in the AT-ZN potential. Blue atoms are self-interstitial atoms (shown as the centres of the Wigner-Seitz cells they belong to). Green lines are $1/2\langle 1\,1\,1\rangle$ dislocation lines and magenta lines are $\langle 1\,0\,0\rangle$ dislocations. The red arrows show the directions of the Burgers vectors. All clusters contain roughly 100 SIAs and are around 3 nm in width.

final cluster is a loop of same type in the majority of the simulations, even in the case of full overlap. At larger separation distances, the probability of the pre-existing cluster surviving naturally approaches unity. Perhaps most interesting is the probability of forming a given cluster type at full overlap, i.e. when the cascade completely dissolves the original cluster and the final cluster type after recrystallisation is dependent on other factors. In the case of the 30 SIA $1/2\langle 1\,1\,1\rangle$ loop in figure 11, the probabilities at full overlap differ noticeably between the two interatomic potentials. In the M07-B potential, a fully overlapping cascade results in a C15-like cluster or a $1/2\langle 1\,1\,1\rangle$ loop with almost equal probability, while C15 clusters only rarely form in the AM04 potential. The observed probabilities agree well with the stabilities of the different types of clusters predicted by the potentials. In Appendix B, the formation energies of loops and C15 clusters are given as functions of the cluster size in the different potentials. At 30 SIAs, the $1/2\langle 1\,1\,1\rangle$ loop is the most stable SIA cluster in the AM04 potential, in contradiction with DFT results that predict the C15 cluster to be the most stable SIA cluster up to around 50 SIAs [19]. In the M07-B potential on the other hand, the crossover in stability between the C15 and $1/2\langle 1\,1\,1\rangle$ loops occurs close to 30 SIAs, and consequently the probability of forming C15 clusters
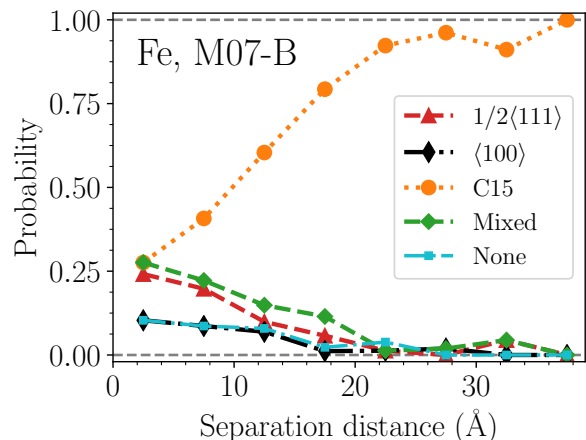
Figure 14: Observed probabilities of forming different types of SIA clusters as functions of separation distance, for 5 keV cascades on a pre-existing 40 SIA C15 cluster at 300 K in the M07-B potential.
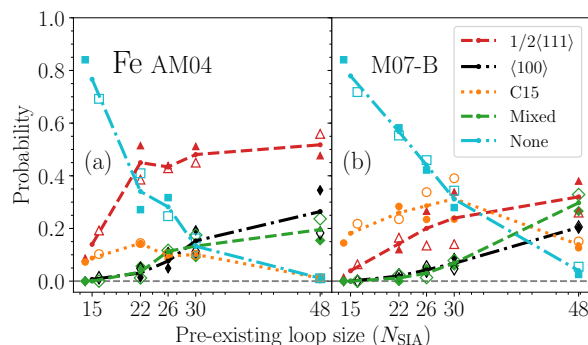

Figure 15: Observed probabilities of forming different types of SIA clusters at full overlap, for 5 keV cascades at 300 K and compared between the AM04 (a) and M07-B (b) potentials. For filled data points, the pre-existing cluster was a $1/2\langle 1\,1\,1\rangle$ loop, and for unfilled data points a $\langle 1\,0\,0\rangle$ loop. The lines connect the average values of both pre-existing loop types.
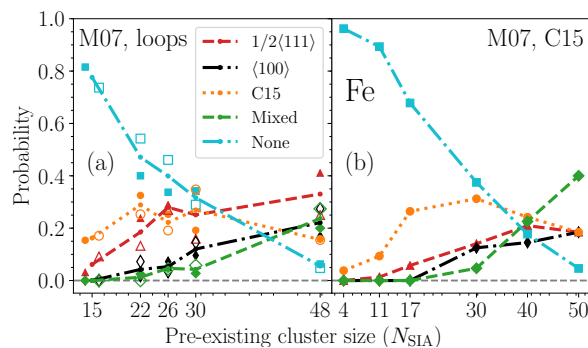

Figure 16: Observed probabilities of forming different types of SIA clusters at full overlap, for 5 keV cascades at 300 K in the M07 potential. In figure (a), the pre-existing clusters are dislocation loops (filled points for pre-existing $1/2\langle 1\,1\,1\rangle$ loops and unfilled points for $\langle 1\,0\,0\rangle$ loops). In figure (b), the pre-existing clusters are C15 clusters.

is significantly higher and similar to the probability of forming $1/2\langle 1\,1\,1\rangle$ loops.

Figure 14 shows the cluster type probabilities as functions of separation distance for a pre-existing 40-SIA C15 cluster in the M07-B potential. At this size, both dislocation loops and the C15 clusters have similar formation energies (Appendix B), with the $1/2\langle 1\,1\,1\rangle$ loop marginally lower in energy than the other types. Consequently, the probabilities of forming the different cluster types at full overlap are similar, with a significant fraction of full-overlap simulations leading to mixed clusters similar to those shown in figure 12. At partial separation distances, the pre-existing C15 cluster survives in the majority of the cases. Nevertheless, partially overlapping cascades also trigger transformations into both types of dislocation loops with non-negligible probabilities.

In figure 15, we show the probabilities of forming different cluster types for fully overlapping cascades on both types of dislocation loops in Fe, compared between the AM04 and M07-B potentials. The effect of the higher stability of the C15 clusters compared to loops in the M07-B potential is clear. In the AM04 potential, C15-like clusters form in around 10% of the full-overlap cases at cluster sizes of 30 SIAs and below, but $1/2\langle 1\,1\,1\rangle$ loops are always the most likely surviving cluster type (except at very small sizes, where the overlapping cascade typically splits the cluster into small parts of only a few or single SIAs). However, in the M07-B potential, C15 clusters are the most frequent identifiable cluster type at sizes below around 30 SIA, after which $1/2\langle 1\,1\,1\rangle$ loops are most likely to form. The crossover coincides with

the crossover in formation energy at 0 K seen in Appendix B. At larger pre-existing cluster sizes, the probability of forming various mixed clusters similar to those shown in figure 12 is also significant. Figure 16 shows the probabilities of forming different clusters in full overlap on pre-existing loops compared with pre-existing C15 clusters. The probabilities are similar in both cases. The only significant difference is an increased probability of forming mixed clusters, at the expense of $1/2\langle 1\,1\,1\rangle$ loops, in overlap with larger C15 clusters. Most of these mixed clusters contain small parts recognisable as C15-like clusters attached to a dislocation loop. Regardless of initial cluster type and interatomic potential, $\langle 1\,0\,0\rangle$ loops are formed

Figure 17: Example of the observed probabilities of forming different types of SIA clusters as functions of separation distance in W. The data is from 10 keV cascades overlapping with a 30 SIA $\langle 1\,0\,0 \rangle$ loop at 300 K in the AT-ZN potential.
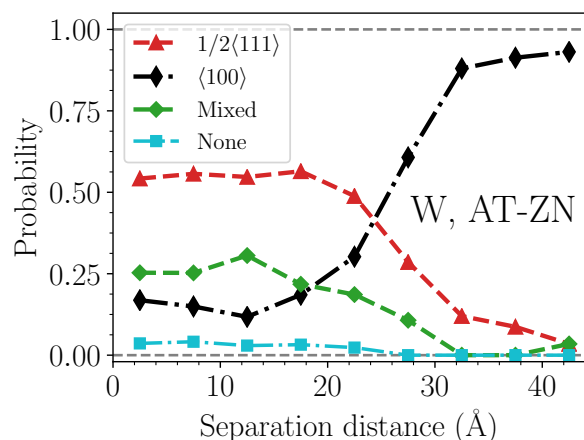

Figure 18: Example of the observed probabilities of forming different types of SIA clusters as functions of separation distance in W. The data is from 10 keV cascades overlapping with a 30 SIA $\langle 1\,0\,0 \rangle$ loop at 300 K in the DND-BN (a) and M4-S (b) potentials.
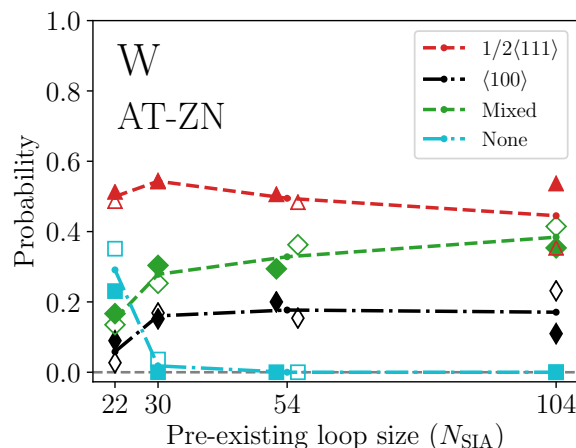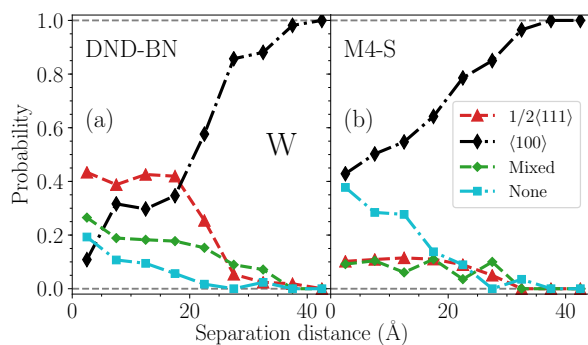

Figure 19: Observed probabilities of forming different types of SIA clusters at full overlap, for 10 keV cascades at 300 K in the AT-ZN potential. For filled data points, the pre-existing cluster was a $1/2\langle 1\,1\,1 \rangle$ loop, and for unfilled data points a $\langle 1\,0\,0 \rangle$ loop. The lines connect the average values of both pre-existing loop types.

with probabilities around 10–20% at sizes above 20 SIAs. Previous simulation results of overlap of 50 keV cascades showed similar probabilities for $\langle 1\,0\,0 \rangle$ loop formation [33].

The formation of different types of clusters in W follow a similar trend as in Fe. That is, the most likely cluster type to form as a result of an overlapping cascade is the cluster with lowest formation energy predicted by the potential, although clusters higher in energy are also seen in non-negligible fractions. However, the relative stability between the two dislocation loops differ significantly between the interatomic potentials. As shown in Appendix B, only the AT-ZN potential correctly predicts $1/2\langle 1\,1\,1 \rangle$ loops

to be lower in energy than $\langle 1\,0\,0 \rangle$ loops. Both the DND-BN and the M4-S potentials contradict DFT data and show a crossover at around 20–30 SIAs, above which $\langle 1\,0\,0 \rangle$ loops become more stable. Consequently, both the latter potentials show high probabilities of forming $\langle 1\,0\,0 \rangle$ loops, while the AT-ZN potential produces $1/2\langle 1\,1\,1 \rangle$ loops in the majority of the overlapping cascades, regardless of the type of the initial pre-existing cluster. This is illustrated for 10 keV cascades overlapping with 30 SIA $\langle 1\,0\,0 \rangle$ loops in figures 17–18. For the DND-BN potential, this is close to the crossover in the relative loop stability, and figure 18 still shows slightly higher fractions of $1/2\langle 1\,1\,1 \rangle$ loops than $\langle 1\,0\,0 \rangle$ loops. In contrast, the M4-S potential only rarely produces $1/2\langle 1\,1\,1 \rangle$ loops. At larger sizes, $\langle 1\,0\,0 \rangle$ loops are the most likely outcome in both the DND-BN and the M4-S potentials, while the AT-ZN potential predominantly produces $1/2\langle 1\,1\,1 \rangle$ loops, as expected based on the relative formation energies. This is similar to previous simulations of high-energy (150 keV) cascades in defect-free W [25], where the AT-ZN potential mainly produced $1/2\langle 1\,1\,1 \rangle$ loops, while both types were frequently seen in the DND-BN potential.

Figure 19 shows the probabilities of forming different cluster at full overlap as a function of pre-existing cluster size in the AT-ZN potential. Due to the incorrect relative stability of loops in the DND-BN and M4-S potentials, we only discuss the results from the AT-ZN potential. Regardless of initial loop type, the resulting cluster after a fully overlapping cascade is roughly independent on size. For all sizes, perfect

$1/2\langle 1\,1\,1\rangle$ loops are the results of about half of the simulations, and $\langle 1\,0\,0\rangle$ loops in around 10–20% of the cases. Interestingly, large fractions (30–40%) of the simulations also end with formation mixed dislocation loops similar to the examples shown in figure 13. All mixed clusters are highly immobile, containing segments of both $\langle 1\,0\,0\rangle$ and $1/2\langle 1\,1\,1\rangle$ dislocation lines of both screw and edge type.

6. Summary and conclusions

From the large number of molecular dynamics simulations performed in this study, a fairly complete picture of the effects of cascade overlap with pre-existing self-interstitial clusters in bcc metals has been obtained. We focused on cascade energies well below the subcascade threshold, overlapping with interstitial clusters smaller than the disordered cascade region. The sizes and types of the pre-existing clusters correspond to clusters typically formed directly in cascades. Under these conditions, the observed effects of cascade overlap with interstitial clusters in iron and tungsten can be summarised as follows.

(i) The number of new Frenkel pairs is reduced to almost zero when a cascade fully overlaps with a SIA cluster of size smaller, but comparable to the disordered cascade region.

(ii) The number of new Frenkel pairs created as a function of the distance between the centre of the disordered cascade region and the pre-existing interstitial cluster follows a simple analytical sigmoid function. The same function, containing no fitting parameters, can be used to estimate the expected number of Frenkel pairs in cascade overlap in both Fe and W, using only data readily obtained from cascades in the defect-free material. The analytical model can be used to introduce cascade-overlap effects in higher-scale simulation methods of radiation damage.

(iii) The size of the pre-existing interstitial cluster decreases as a result of a fully overlapping cascade. The decrease in number of interstitials in the cluster was found to be mostly dependent on PKA energy and temperature, with no dependence on the size of the initial cluster. The cascade-induced changes in cluster size is strongly stochastic, and an interstitial cluster can also absorb a small number of new interstitials created by a nearby cascade that is not, or is only slightly, overlapping.

(iv) The Burgers vector or type of the pre-existing cluster may change as a result of cascade overlap. Although the lowest-energy cluster type is the most likely to form, higher-energy clusters are also formed with significant probabilities. Most notably, in Fe, cascade-induced transformations from C15 clusters and $1/2\langle 1\,1\,1\rangle$ loops into $\langle 1\,0\,0\rangle$ dislocation loops are observed with 10–20% probabilities at full overlap. The surviving cluster type is, however, strongly dependent on the interatomic potential. Many interatomic potentials fail to reproduce the relative stability of SIA clusters, which as our results show have a direct effect on the outcome of overlapping cascades. Our results therefore emphasise the continuous demand for more accurate interatomic potentials.

(v) We found that the C15 cluster is highly stable in Fe, and survives an overlapping cascade in the majority of cases. Nevertheless, as the size of the C15 cluster increases, cascade-induced collapse into either $1/2\langle 1\,1\,1\rangle$ or $\langle 1\,0\,0\rangle$ dislocation loops become increasingly likely. This indicates that the previously proposed mechanism of $\langle 1\,0\,0\rangle$ loop formation from C15 collapse in iron can be triggered by a nearby cascade at sizes much smaller than the critical sizes observed in pure growth simulations [31]. Furthermore, given that the stability of C15 clusters in all interatomic potentials are underestimated compared to ab initio data, formation and transformation of clusters into C15 is likely even more frequent than observed here.

(vi) The relatively frequent observations of $\langle 1\,0\,0\rangle$ loops in our simulations indicate that, regardless of mechanism, cascade overlap is likely to accelerate the formation of $\langle 1\,0\,0\rangle$ loops. This is supported by experimental observations of increased densities of $\langle 1\,0\,0\rangle$ loops at higher doses [23].

(vii) In W, cascade-induced changes between $1/2\langle 1\,1\,1\rangle$ and $\langle 1\,0\,0\rangle$ loops are also frequently observed, but the differences between predictions of different interatomic potentials are large.
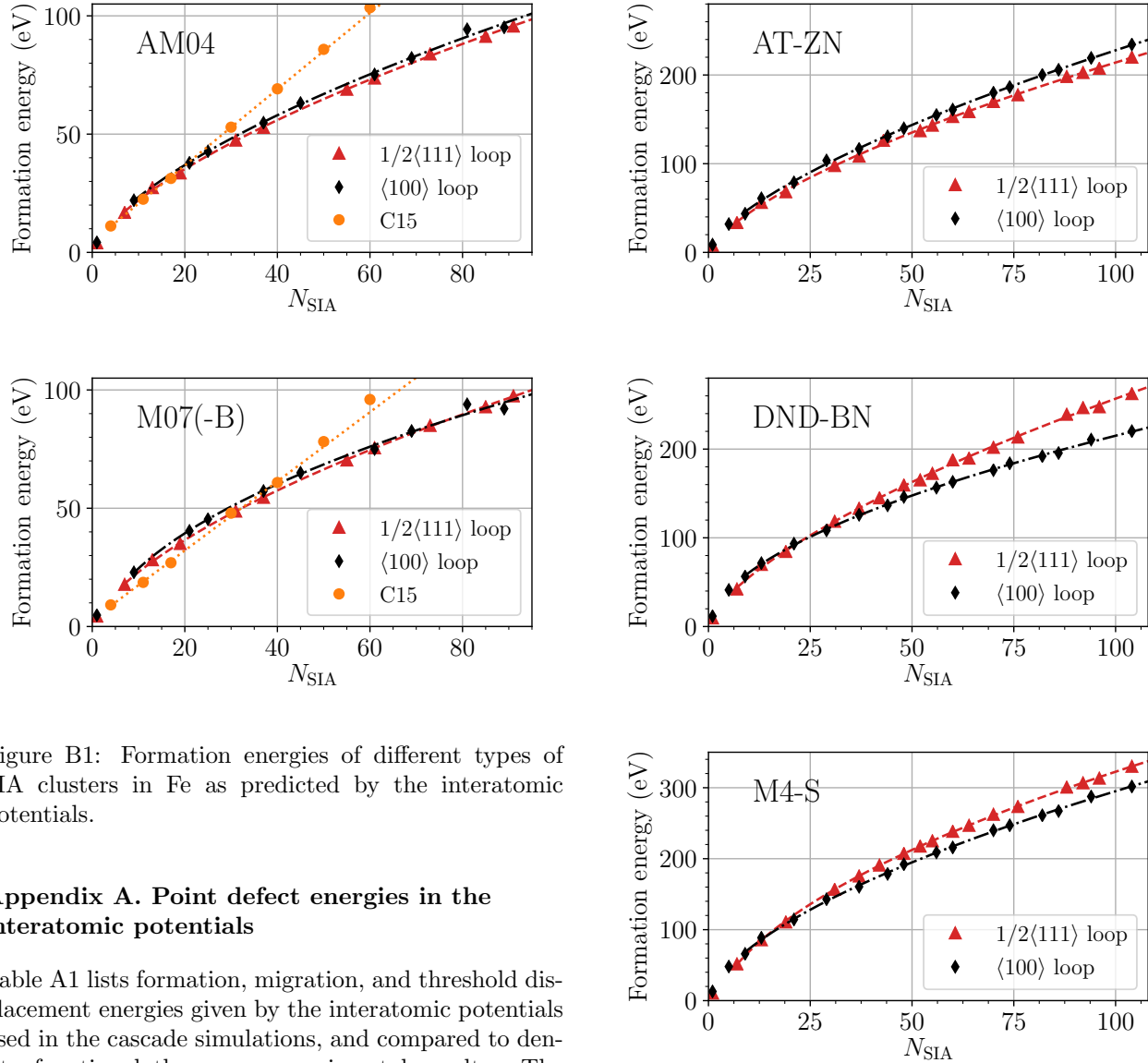
Figure B1: Formation energies of different types of SIA clusters in Fe as predicted by the interatomic potentials.

Appendix A. Point defect energies in the interatomic potentials

Table A1 lists formation, migration, and threshold displacement energies given by the interatomic potentials used in the cascade simulations, and compared to density functional theory or experimental results. The formation energies of the self-interstitial and vacancy were calculated following a minimisation of energy and pressure. The migration energies were obtained using the nudged elastic band method as implemented in ASE [54]. The threshold displacement energies are taken from earlier studies [21, 42, 44].

Appendix B. Formation energies of SIA clusters in Fe and W

Figures B1 and B2 show the formation energies of the different SIA clusters in Fe and W as given by the interatomic potentials used in the cascade simulations. Note that the M07 and M07-B potentials predict identical formation energies, since the potentials only differ at distances shorter than those present in any stable SIA cluster. The systems containing the dislocation loop or C15 cluster were minimised in

Figure B2: Formation energies of SIA dislocation loops in W as predicted by the interatomic potentials.

energy and pressure using the conjugate gradient algorithm implemented in LAMMPS [60]. The lines connecting the data point are fits to the corresponding formation energy scaling laws discussed in [19]. For dislocation loops, the formation energy scales according to

$$E_\mathrm{f} = a_0\sqrt{N}\ln(N) + a_1\sqrt{N} + a_2, \qquad (B.1)$$

where N is the number of interstitial atoms (or vacancies) in the dislocation loop, and a_i are used as fitting parameters. For C15 clusters, the formation energy scales as

$$E_\mathrm{f} = a_0 N^{2/3} + a_1 N + a_2. \qquad (B.2)$$

Table A1: Formation energies (E_f), migration energies (E_m), and threshold displacement energies (E_d) in eV, predicted by the different interatomic potentials and compared to density functional theory (DFT) and experimental data. Only the energies of the lowest-energy interstitial configuration are given ($\langle 1\,1\,0\rangle$ dumbbell in Fe and $\langle 1\,1\,1\rangle$ dumbbell in W).

Fe				
	DFT	AM04	M07	M07-B
$E_\mathrm{f}^\mathrm{SIA}$	3.64–4.25[a,b]	3.52	3.69	3.69
$E_\mathrm{f}^\mathrm{vac}$	2.09[b]	1.71	2.10	2.10
$E_\mathrm{m}^\mathrm{SIA}$	0.34[c]	0.31	0.30	0.30
$E_\mathrm{m}^\mathrm{vac}$	0.67[c]	0.64	0.69	0.69
$E_\mathrm{d}^{\langle 1\,0\,0\rangle}$	21[b]	17[d]	27[d]	17[d]
$E_\mathrm{d}^{\langle 1\,1\,0\rangle}$	43[b]	33[d]	51[d]	39[d]
$E_\mathrm{d}^{\langle 1\,1\,1\rangle}$	20[b]	29[d]	43[d]	33[d]
$E_\mathrm{d}^\mathrm{avg}$	32[b]	39.6 ± 0.2[d]	65.5 ± 0.3[d]	39.2 ± 0.2[d]
W				
	DFT/exp.	AT-ZN	DND-BN	M4-S
$E_\mathrm{f}^\mathrm{SIA}$	9.55[e]; 10.53[f]	7.77	9.45	10.39
$E_\mathrm{f}^\mathrm{vac}$	3.56[e]; 3.49[f]	3.63	3.56	3.82
$E_\mathrm{m}^\mathrm{SIA}$	0.05[e]; 0.002[g]	0.032	0.012	0.023
$E_\mathrm{m}^\mathrm{vac}$	1.78[e]	1.44	2.06	1.83
$E_\mathrm{d}^{\langle 1\,0\,0\rangle}$	42 ± 1[h]	57[i]	41[j]	43[i]
$E_\mathrm{d}^{\langle 1\,1\,0\rangle}$	>70[h]	103[i]	93[j]	71[i]
$E_\mathrm{d}^{\langle 1\,1\,1\rangle}$	44 ± 1[h]	89[i]	41[j]	65[i]

[a] Ref. [37] [b] Ref. [55] [c] Ref. [56] [d] Ref. [21]
[e] Ref. [57] [f] Ref. [43] [g] Ref. [58] [h] Ref. [59]
[i] Ref. [44] [j] Ref. [42]

In Fe, both potentials correctly predict the C15 cluster to be lowest in energy at small sizes. However, the differences in energy between the clusters in AM04 potential are very small, and loops become more stable at around 20 SIA. In the M07(-B) potentials, the crossover from C15 to $1/2\langle 1\,1\,1\rangle$ loops is at around 30 SIA, and to $\langle 1\,0\,0\rangle$ loops at around 40 SIA. Note, however, that the number of different possible C15 configurations grows quickly with size, and here we only considered a few configurations for each size (figure B1 only shows the lowest-energy configurations at each size). The crossovers might therefore be underestimated. However, approximate values are sufficient for interpreting the cascade-overlap results presented here, and a detailed benchmarking of interatomic potentials for SIA clusters is beyond the scope of this work. The crossover between C15 and $1/2\langle 1\,1\,1\rangle$ loops is predicted to be around 51 SIA based on density functional theory data [19], and around 91 SIA for C15 and $\langle 1\,0\,0\rangle$ loops. The M07(-B) potentials also predict a crossover between the the two loop types at around 80 SIA. This contradicts density functional theory data, which predicts the $1/2\langle 1\,1\,1\rangle$ loops to be lower in energy at all sizes [19].

As in Fe, $1/2\langle 1\,1\,1\rangle$ loops in W should also be lower in energy than $\langle 1\,0\,0\rangle$ loops at all sizes [19]. Among the interatomic potentials used in this study, only the AT-ZN potential reproduces this trend, as seen in figure B2. The crossover between the loop types is at around 25 SIA in the DND-BN potential and at around 20 SIA in the M4-S potential, above which $\langle 1\,0\,0\rangle$ loops incorrectly are more stable.

Appendix C. Data from cascades in defect-free Fe and W

Table C1 lists the data extracted from cascades in defect-free Fe and W using the same PKA energies, temperatures, and interatomic potentials as in the overlapping cascades. The data is used as input parameters for the analytical model of Frenkel-pair production in cascade overlap.

References

[1] Hernández-Mayoral M, Yao Z, Jenkins M L and Kirk M A 2008 *Philos. Mag.* **88** 2881–2897 ISSN 1478-6435
[2] Jenkins M L, Yao Z, Hernández-Mayoral M and Kirk M A

Table C1: Data from single cascades in defect-free Fe and W for the same PKA energies (E_{PKA}), temperatures, and interatomic potentials as in the overlapping cascades in the main text. 50 simulations were carried out for each case. N_{p} is the number of Frenkel pairs created after the cascades, given by the mean values and standard errors, with the median values in brackets. V_{c} is the average volume of the cascade-induced liquid region at peak damage, and r_{c} is the corresponding radius assuming a spherical cascade volume.

Fe					
Potential	E_{PKA} (keV)	T (K)	N_{p}	V_{c} (Å^3)	r_{c} (Å)
AM04	3	0	9.0 ± 0.4 (9)	10531	13.5
AM04	3	300	8.2 ± 0.3 (8)	13612	14.7
AM04	5	0	13.1 ± 0.5 (12)	18352	16.3
AM04	5	300	10.8 ± 0.4 (11)	23092	17.6
M07	3	0	7.5 ± 0.3 (8)	7806	12.2
M07	3	300	6.3 ± 0.2 (6.5)	9518	13.0
M07	5	0	11.2 ± 0.3 (11)	13750	14.7
M07	5	300	9.6 ± 0.3 (10)	16060	15.6
M07-B	3	0	11.5 ± 0.4 (11.5)	7935	12.3
M07-B	3	300	9.4 ± 0.4 (9.0)	10211	13.3
M07-B	5	0	16.2 ± 0.5 (16.5)	13389	14.6
M07-B	5	300	12.8 ± 0.5 (12)	16575	15.7
W					
Potential	E_{PKA} (keV)	T (K)	N_{p}	V_{c} (Å^3)	r_{c} (Å)
AT-ZN	10	0	8.7 ± 0.3 (8)	27923	18.8
AT-ZN	10	300	8.6 ± 0.3 (8)	29943	19.2
AT-ZN	30	0	19.3 ± 0.7 (19)	104178	29.2
AT-ZN	30	300	19.2 ± 0.7 (18.5)	111186	29.8
DND-BN	10	0	10.8 ± 0.4 (10.5)	25494	18.2
DND-BN	10	300	8.9 ± 0.3 (9)	27966	18.8
DND-BN	30	0	23.9 ± 0.9 (22)	95293	28.3
DND-BN	30	300	21.2 ± 0.8 (21.5)	106119	29.3
M4-S	10	0	11.6 ± 0.5 (10.5)	20801	17.0
M4-S	10	300	11.0 ± 0.5 (10)	23311	17.7
M4-S	30	0	24.9 ± 0.9 (24)	80322	26.8
M4-S	30	300	21.8 ± 0.7 (21)	86295	27.4

2009 *Journal of Nuclear Materials* **389** 197–202 ISSN 0022-3115

[3] Yao Z, Jenkins M L, Hernández-Mayoral M and Kirk M A 2010 *Philos. Mag.* **90** 4623–4634 ISSN 1478-6435

[4] Yi X, Jenkins M L, Hattar K, Edmondson P D and Roberts S G 2015 *Acta Materialia* **92** 163–177 ISSN 1359-6454

[5] Zinkle S and Snead L 2014 *Annu. Rev. Mater. Res.* **44** 241–267

[6] Stork D, Agostini P, Boutard J L, Buckthorpe D, Diegele E, Dudarev S L, English C, Federici G, Gilbert M R, Gonzalez S, Ibarra A, Linsmeier C, Puma A L, Marbach G, Packer L W, Raj B, Rieth M, Tran M Q, Ward D J and Zinkle S J 2014 *Fusion Engineering and Design* **89** 1586–1594 ISSN 0920-3796

[7] Knaster J, Moeslang A and Muroga T 2016 *Nat Phys* **12** 424–434 ISSN 1745-2473

[8] Nordlund K, Zinkle S J, Sand A E, Granberg F, Averback R S, Stoller R E, Suzudo T, Malerba L, Banhart F, Weber W J, Willaime F, Dudarev S L and Simeone D 2018 *Journal of Nuclear Materials* **512** 450–479 ISSN 0022-3115

[9] Soneda N and de la Rubia T D 1998 *Philosophical Magazine A* **78** 995–1019

[10] Souidi A, Becquart C, Domain C, Terentyev D, Malerba L, Calder A, Bacon D, Stoller R, Osetsky Y N and Hou M 2006 *J. Nucl. Mater.* **355** 89–103 ISSN 0022-3115

[11] Mason D R, Yi X, Kirk M A and Dudarev S L 2014 *J. Phys. Condens. Matter* **26** 375701

[12] Castin N, Bakaev A, Bonny G, Sand A, Malerba L and Terentyev D 2017 *Journal of Nuclear Materials* **493** 280–293 ISSN 0022-3115

[13] Dunn A and Capolungo L 2015 *Computational Materials Science* **102** 314–326 ISSN 0927-0256

[14] Gao F, Bacon D J, Calder A F, Flewitt P E J and Lewis T A 1996 *Journal of Nuclear Materials* **230** 47–56 ISSN 0022-3115

[15] Stoller R E and Guiriec S G 2004 *Journal of Nuclear Materials* **329–333, Part B** 1238–1242 ISSN 0022-3115

[16] Terentyev D, Vörtler K, Björkas C, Nordlund K and Malerba L 2011 *Journal of Nuclear Materials* **417** 1063–1066 ISSN 0022-3115

[17] Sand A E, Byggmästar J, Zitting A and Nordlund K 2018 *Journal of Nuclear Materials* **511** 64–74 ISSN 0022-3115

[18] Marinica M C, Willaime F and Crocombette J P 2012 *Phys. Rev. Lett.* **108** 025501

[19] Alexander R, Marinica M C, Proville L, Willaime F,

Arakawa K, Gilbert M R and Dudarev S L 2016 *Phys. Rev. B* **94** 024103

[20] Dérès J, Proville L and Marinica M C 2015 *Acta Materialia* **99** 99–105 ISSN 1359-6454

[21] Byggmästar J, Granberg F and Nordlund K 2018 *Journal of Nuclear Materials* **508** 530–539 ISSN 0022-3115

[22] Masters B C 1965 *Philos. Mag.* **11** 881–893 ISSN 0031-8086

[23] Schäublin R, Décamps B, Prokhodtseva A and Löffler J F 2017 *Acta Materialia* **133** 427–439 ISSN 1359-6454

[24] Yi X, Jenkins M L, Briceno M, Roberts S G, Zhou Z and Kirk M A 2013 *Philos. Mag.* **93** 1715–1738 ISSN 1478-6435

[25] Sand A E, Dudarev S L and Nordlund K 2013 *EPL* **103** 46003 ISSN 0295-5075

[26] Dudarev S L, Bullough R and Derlet P M 2008 *Phys. Rev. Lett.* **100** 135503

[27] Marian J, Wirth B D and Perlado J M 2002 *Phys. Rev. Lett.* **88** 255507

[28] Xu H, Stoller R E, Osetsky Y N and Terentyev D 2013 *Phys. Rev. Lett.* **110** 265503

[29] Arakawa K, Hatanaka M, Kuramoto E, Ono K and Mori H 2006 *Phys. Rev. Lett.* **96** 125506

[30] Gao N, Chen J, Kurtz R J, Wang Z G, Zhang R F and Gao F 2017 *J. Phys.: Condens. Matter* **29** 455301 ISSN 0953-8984

[31] Zhang Y, Bai X M, Tonks M R and Biner S B 2015 *Scripta Materialia* **98** 5–8 ISSN 1359-6462

[32] Peng Q, Meng F, Yang Y, Lu C, Deng H, Wang L, De S and Gao F 2018 *Nat. Commun.* **9** 4880 ISSN 2041-1723

[33] Granberg F, Byggmästar J, Sand A E and Nordlund K 2017 *EPL* **119** 56003 ISSN 0295-5075

[34] Nordlund K, Ghaly M, Averback R S, Caturla M, Diaz de la Rubia T and Tarus J 1998 *Phys. Rev. B* **57** 7556–7570

[35] Ghaly M, Nordlund K and Averback R S 1999 *Philos. Mag. A* **79** 795–820 ISSN 0141-8610

[36] Ackland G J, Mendelev M I, Srolovitz D J, Han S and Barashev A V 2004 *J. Phys.: Condens. Matter* **16** S2629 ISSN 0953-8984

[37] Malerba L, Marinica M C, Anento N, Björkas C, Nguyen H, Domain C, Djurabekova F, Olsson P, Nordlund K, Serra A, Terentyev D, Willaime F and Becquart C S 2010 *Journal of Nuclear Materials* **406** 19–38 ISSN 0022-3115

[38] Ackland G J and Thetford R 1987 *Philos. Mag. A* **56** 15–30 ISSN 0141-8610

[39] Zhong Y, Nordlund K, Ghaly M and Averback R S 1998 *Phys. Rev. B* **58** 2361–2364

[40] Derlet P M, Nguyen-Manh D and Dudarev S L 2007 *Phys. Rev. B* **76** 054107

[41] Ziegler J F, Biersack J P and Littmarck U 1985 The Stopping and Range of Ions in Matter *Treatise on Heavy-Ion Science* (New York: Pergamon) pp 93–129 ISBN 978-1-4615-8105-5 978-1-4615-8103-1

[42] Björkas C, Nordlund K and Dudarev S 2009 *Nuclear Instruments and Methods in Physics Research Section B: Beam Interactions with Materials and Atoms* **267** 3204–3208 ISSN 0168-583X

[43] Marinica M C, Ventelon L, Gilbert M R, Proville L, Dudarev S L, Marian J, Bencteux G and Willaime F 2013 *J. Phys.: Condens. Matter* **25** 395502 ISSN 0953-8984

[44] Sand A E, Dequeker J, Becquart C S, Domain C and Nordlund K 2016 *Journal of Nuclear Materials* **470** 119–127 ISSN 0022-3115

[45] Berendsen H J C, Postma J P M, van Gunsteren W F, DiNola A and Haak J R 1984 *J. Chem. Phys.* **81** 3684–3690 ISSN 0021-9606, 1089-7690

[46] Björkas C and Nordlund K 2009 *Nucl. Instr. and Meth. B* **267** 1830 – 1836 ISSN 0168-583X

[47] Sand A E, Dudarev S L and Nordlund K 2013 *EPL* **103** 46003

[48] Sand A and Nordlund K 2015 *J. Nucl. Mater.* **456** 99–105 ISSN 0022-3115

[49] Vörtler K, Björkas C, Terentyev D, Malerba L and Nordlund K 2008 *Journal of Nuclear Materials* **382** 24–30 ISSN 0022-3115

[50] Stukowski A 2010 *Modelling Simul. Mater. Sci. Eng.* **18** 015012 ISSN 0965-0393 http://ovito.org/

[51] Stukowski A, Bulatov V V and Arsenlis A 2012 *Modelling Simul. Mater. Sci. Eng.* **20** 085007 ISSN 0965-0393

[52] Backer A D, Sand A E, Nordlund K, Luneville L, Simeone D and Dudarev S L 2016 *EPL (Europhysics Letters)* **115** 26001

[53] Sand A E, Mason D R, Backer A D, Yi X, Dudarev S L and Nordlund K 2017 *Materials Research Letters* **5** 357–363

[54] Larsen A H, Mortensen J J, Blomqvist J, Castelli I E, Christensen R, Marcin Dułak, Friis J, Groves M N, Hammer B, Hargus C, Hermes E D, Jennings P C, Jensen P B, Kermode J, Kitchin J R, Kolsbjerg E L, Kubal J, Kristen Kaasbjerg, Lysgaard S, Maronsson J B, Maxson T, Olsen T, Pastewka L, Andrew Peterson, Rostgaard C, Schiøtz J, Schütt O, Strange M, Thygesen K S, Tejs Vegge, Vilhelmsen L, Walter M, Zeng Z and Jacobsen K W 2017 *J. Phys.: Condens. Matter* **29** 273002 ISSN 0953-8984

[55] Olsson P, Becquart C S and Domain C 2016 *Mater. Res. Lett.* **4** 219–225 ISSN null

[56] Fu C C, Torre J D, Willaime F, Bocquet J L and Barbu A 2005 *Nat. Mater.* **4** 68–74 ISSN 1476-4660

[57] Nguyen-Manh D, Horsfield A P and Dudarev S L 2006 *Phys. Rev. B* **73** ISSN 1098-0121, 1550-235X

[58] Swinburne T D, Ma P W and Dudarev S L 2017 *New J. Phys.* **19** 073024 ISSN 1367-2630

[59] Maury F, Biget M, Vajda P, Lucasson A and Lucasson P 1978 *Radiat. Eff.* **38** 53–65 ISSN 0033-7579

[60] Plimpton S 1995 *Journal of Computational Physics* **117** 1–19 ISSN 0021-9991 http://lammps.sandia.gov